

Surface Stress with Non-stationary Weak Winds and Stable Stratification

L. Mahrt¹ · Christoph K. Thomas²

Received: 30 April 2015 / Accepted: 6 November 2015 / Published online: 27 November 2015
© Springer Science+Business Media Dordrecht 2015

Abstract The behaviour of turbulent transport in the weak-wind, stably-stratified, boundary layer over land is examined in terms of the non-stationarity of the wind field using measurements from three field programs. These field programs include towers ranging from 12 to 20 m in height and an extensive horizontal network of sonic anemometers. The relationship of the friction velocity to the stratification and non-stationary submeso motions is investigated from several points of view and nominally quantified. The relationship of the turbulence to the stratification is less systematic than expected partly due to enhancement of the turbulence by submeso motions. Cause and effect relationships are difficult to isolate because the non-stationary momentum flux significantly modifies the profile of the non-stationary mean flow. The link between the turbulence and accelerations at the surface is examined in terms of the changing vertical structure of the wind profile and sudden increases in the downward transport of momentum.

Keywords Nocturnal boundary layer · Non-stationarity · Stable boundary layer · Stratified turbulence · Submeso

1 Introduction

Some studies have found that the relationship between turbulence and stratification in the nocturnal boundary layer is more obscure or indirect than originally expected (Sun et al. 2012). Liang et al. (2014) find no significant dependence of the turbulence on the stratification for small wind speeds even for strong stability. These studies are part of an increasing trend questioning the usefulness of traditional thinking in the atmospheric boundary layer with significant stratification (Hicks et al. 2014).

✉ L. Mahrt
mahrt@nwra.com

¹ NorthWest Research Associates, 2171 NW Kari Pl, Corvallis, OR 97330, USA

² Micrometeorology Group, University of Bayreuth, 95540 Bayreuth, Germany

The turbulence for stable stratification is observed to increase slowly with increasing wind speed until the speed reaches a transition or threshold value (Sun et al. 2012). The turbulence increases more rapidly with increasing wind speed for wind speeds greater than this transition value. As a result of the weak relationship of the turbulence to the wind speed and stratification for small wind speeds, the turbulence shows only a very weak dependence on the Richardson number for large values of the Richardson number (e.g., Sorbjan and Grachev 2010; Thomas et al. 2013). There is no critical gradient Richardson number that corresponds to a complete collapse of the turbulence (Galperin et al. 2007).

The generally weak relationship between the turbulence and stratification for small wind speeds might be in part due to non-stationarity (Liang et al. 2014) associated with generation of the turbulence by accelerating submeso motions (Mahrt 2010b; Sun et al. 2015; Vercauteren and Klein 2015). For example, the turbulence can be enhanced by non-stationary distortion of wind profiles (Mahrt et al. 2013) where such distortion includes transient near-surface wind maxima and inflection points (Kang et al. 2015). This situation corresponds to one of two types of submeso regimes in very stable conditions (Vercauteren and Klein 2015) where there is no spectral gap between the turbulence and the smallest scale submeso motions. Enhanced turbulence is most clearly evident in the somewhat different problem of a local maximum of the turbulence intensity as the turbulence adjusts to an increase of surface roughness (Garratt 1990, 1994).

Some of the non-turbulent submeso motions responsible for the turbulence are inadvertently excluded from the computed mean flow with traditional averaging windows of 5 min or more. Vercauteren and Klein (2015) found a second type of submeso regime where wave-like motions occurred only on scales significantly larger than the turbulent scales corresponding to a partial spectral gap. With this regime, the turbulence is expected to better maintain equilibrium with the submeso flow because the time scale of the submeso motion for this regime is likely to be larger than the turbulent adjustment time scale.

Submeso motions include locally-driven propagating modes such as wave-like motions, density currents (Soler et al. 2014) and complex structures of unknown origin. Kang et al. (2015) found that submeso structures in stratified flow are typically wave-like with significant wind speeds but tend to take on a microfront signature with very small wind speeds that include non-stationary near-surface wind maxima and inflection points in the wind profile. Such submeso modes introduce a site dependence (Thomas 2011; Acevedo et al. 2014) and at the same time prevent a completely local solution. The potentially large domain of the origin of the submeso motions determines the region of influence on the local turbulence. This domain can also be deep through the vertical propagation of waves (Finnigan 1999).

The downward mixing of turbulence from higher levels for small wind speeds degrades the relationship of the turbulence to the local stratification and wind speed (Sun et al. 2012; Williams et al. 2013). Based on direct numerical simulation (DNS) for strong stability, Shah and Bou-Zeid (2014) found that with strong stability the near-surface flow often accelerates due to downward turbulent mixing in which case the turbulent momentum flux drives the surface wind accelerations. This contrasts with the usual boundary-layer concept where near-surface flow accelerations drive an increase of turbulence and momentum flux.

van Hooijdonk et al. (2015) point out the disadvantage of evaluating turbulent relationships at a single level because the shear over a layer of finite thickness generates the turbulence. Sun et al. (2012) argue that the surface-based shear instability is confined to levels below the observational height when the wind speed at the observational height is below a height-dependent threshold value. The depth of shear instability becomes greater and encompasses the observational level when the wind speed becomes larger than the transition value. Defining the appropriate depth for observations is difficult due to the simultaneous importance of fine-

scale turbulence (Mahrt et al. 2014) and the potential development of large eddies, as found in DNS of stably-stratified Ekman flow (Anson and Mellado 2014).

In the present study, we examine the relationship between the turbulence and the submeso motions for wind speeds smaller than the transition value using measurements from three field programs. The Shallow Cold Pool (SCP) field program was conducted over gentle topography in a semi-arid grassland of north-eastern Colorado, USA. The FLuxes Over Snow Surfaces II (FLOSSII) experiment took place on relatively flat terrain in a broad valley in north-central Colorado, USA. The field program at the Botany and Plant Pathology (BPP) farm of Oregon State University near Corvallis, Oregon, USA is characterized by a locally flat heterogeneous surface. All three sites are heterogeneous to different degrees and advection may be important. For weak-wind, stably-stratified, flows the weak turbulence permits significant influence of even weak surface heterogeneity. The corresponding horizontal temperature gradients induce baroclinity that potentially modifies the wind profiles. Statistical uncertainty is a necessary shortcoming of the examination of small wind speeds with stable stratification, which are typically non-stationary with intermittent turbulence, as discussed in Sect. 3.2.

2 Measurements

Our study analyzes sonic anemometer measurements at 1 m above the ground and from a central tower in each of the three programs.

2.1 Shallow Cold Pool Experiment

The SCP field program was conducted over semi-arid grasslands in north-eastern Colorado, USA at approximately 1660 m above sea level from 1 October to 1 December 2012. Details can be found at https://www.eol.ucar.edu/field_projects/scp. The primary goal of the field program was to examine transient drainage flows and cold pools over common shallow topography (Mahrt et al. 2014). The main valley is relatively small, typically 12 m deep, 270 m across and roughly 1 km long. The width of the valley bottom averages about 5 m with an average down-valley slope of 2 %, increasing to about 3 % in the up-valley tributary gullies. The side slopes of the valley are on the order of 10 % or less.

Our study analyzes primarily 1-m sonic anemometer measurements (ModelCSAT3, Campbell Scientific, Logan, Utah, USA) from 19 stations and from the main tower between 1700 local standard time to 0700 local standard time the following day. Our study also analyzes 1-Hz temperature measurements from NCAR hygrothermometers deployed at the 0.5- and 2-m levels at the 19 stations. The temperature measurements from the hygrothermometers are more accurate than the temperature measurements from the 1-m sonic anemometers and are used here to compute the bulk vertical temperature difference. Near-neutral conditions are eliminated by discarding data where $\delta\theta$, the difference in potential temperature between 0.5 and 2 m, is less than 0.5 K. The stratification is always represented as $\delta\theta$ using the 0.5- and 2-m measurements. Flux uncertainties for very small wind speeds are briefly discussed in Mahrt et al. (2015). For the high plains SCP field site, windy conditions were commonly observed at the 20-m level. In addition, 20 % of the nights were overcast and few nights were clear the entire night.

2.2 The FLOSSII Field Program

Sonic anemometer measurements were collected in North Park, Colorado, USA in 2002, during the Fluxes Over a Snow Surface II (FLOSSII, <http://www.eol.ucar.edu/isf/projects/>

FLOSSII) experiment within a broad deep valley (Mahrt 2010a). On average, the valley floor is about 30 km wide with valley sidewalls of 1,000 m over a horizontal width of about 7 km. The valley sidewalls vary substantially along the valley and between the two sidewalls. The weak down-valley slope is toward the north, although local undulations in the valley floor may dominate the local slope. A typical down-valley slope is about 1 %, although the estimation of the down-valley slope is sensitive to the choice of horizontal scale. The surface consists of matted grass, sometimes with a shallow snow cover; the aerodynamic roughness length for this site is quite small, less than 1 mm with snow cover. The wind speeds were generally large at this high altitude site and the 1-m wind speed was $<1 \text{ m s}^{-1}$ only 17 % of the time. Data are analyzed between 1900 and 0500 LST. The stratification $\delta\theta$ is again computed as the difference in potential temperature between the 0.5- and 2-m levels.

2.3 The BPP Field Program

The BPP site (Thomas et al. 2012) is located on the Botany and Plant Pathology Farm of Oregon State University with the observations analyzed here collected from late August until mid-October 2011. This site consists of a network of instruments located within a grass-covered shallow depression 20 m across and roughly 50 m long and about 1 m deep, framed by micro-slopes on the order of 5 %. This observational domain is embedded within a larger flat region of mixed agriculture that includes vineyards, orchards and isolated buildings. Wind speeds were generally quite small and the 1-m wind speed was $<1 \text{ m s}^{-1}$ more than half of the time.

The turbulence was measured at 10 Hz with R. M. Young 81000 VRE sonic anemometers. The roughness length is wind-direction dependent but always greater than about 25 mm. For representative 1-m measurements, we use data from station C3 that are thought to be the least affected by surface structures near the network, though our conclusions are not sensitive to this choice. The temperature profile at the BPP site is evaluated from 10 aspirated Omega TMTSS-020G thermocouples deployed on the 12-m tower; see Thomas and Smoot (2013) for an evaluation of the radiation shields used in this field program. The stratification $\delta\theta$ is computed from the 0.8-m and 3.0-m thermistors. No attempt was made to fit the thermocouple profiles in order to estimate the 0.5–2.0 m temperature difference that is measured at the other sites. The vertical temperature difference is computed over a layer of 2.2-m thickness instead of 1.5 m for the other two sites, which would act to increase the temperature difference. The temperature difference for the BPP analysis is centered at a higher level above the ground compared to the other sites, which decreases the temperature difference (the vertical temperature differences decreases rapidly with height). Therefore, the temperature difference for the BPP analysis is reported without any adjustments. Data are analyzed between 2100 and 0600 LST.

3 Averaging Strategies

3.1 Averaging Time

Small wind speeds in the nocturnal boundary layer are generally significantly non-stationary including small-scale non-turbulent motions on time scales just larger than the largest turbulent eddies. Here, such small-scale, non-turbulent, motions are considered to be part of the mean flow for the application of Reynolds averaging. The averaging time, τ , is ideally defined to include the largest turbulent eddies as perturbations but exclude non-turbulent motions as

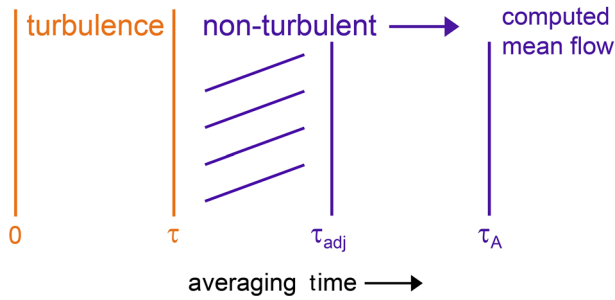


Fig. 1 One common scenario of the relationship between time scales where τ_{adj} is the turbulent adjustment time scale required by the turbulence to adjust to new conditions, and τ_A is the averaging time. Optimally, the averaging time τ_A is chosen as the largest turbulent time scale (τ). This sketch shows a more traditional choice of the averaging time τ_A that is larger than the largest turbulent scale, at least for weak-wind stratified conditions

perturbations. Separation of the turbulence from the non-turbulent flow for non-stationary weak winds is not as clear compared to fully-developed turbulence driven by stationary flow where a spectral gap assists in the choice of the averaging time.

Choice of an averaging time τ_A greater than the time scale of the largest turbulent eddies (τ) leads to perturbation quantities that include non-turbulent motions on time scales between τ and τ_A (Fig. 1). This choice is common in the weak-wind, stably-stratified, boundary layer where the turbulence is confined to very small time scales. Choice of $\tau_A > \tau$ also leads to a computed mean flow that omits some of the non-turbulent flow responsible for the generation of turbulence.

The non-turbulent flow on time scales just larger than the turbulent scales and smaller than the turbulent adjustment time scale τ_{adj} (Fig. 1, hatched area) generates turbulence that does not maintain equilibrium with the non-turbulent flow. The turbulent adjustment time describes the time required for turbulence to adjust to a change of mean flow conditions. The adjustment time scale for decreased forcing of the turbulence is commonly formulated in terms of the dissipation time scale (Tennekes and Lumley 1972). However, in general, it is not obvious how to numerically define τ_{adj} from atmospheric observations, so Fig. 1 is more conceptual than quantitative and identifies a band of time scales where the non-stationary submeso motions prevent turbulence equilibrium.

For the SCP field program, Mahrt et al. (2015) found a 10–15 % reduction in the downward heat flux based on 10-s averaging lengths compared to 5-min averaging lengths for $V > 4 \text{ m s}^{-1}$ where V is the speed of the vector-averaged flow. Our study emphasizes wind speeds $< \text{a few m s}^{-1}$ in which case the loss of heat flux for the 10-s averages is small. Unless otherwise noted, our study uses a 10-s averaging window for the SCP field program to approximate τ_A and reduce contamination of the fluctuations by the non-turbulent motions. This choice of small τ_A provides a more concise measure of the turbulence and this averaging time resolves the smallest-scale non-turbulent motions as part of the mean flow. Because the time scale of the large turbulent eddies increases with height, examination of the vertical structure of the fluxes across the tower layer (Sect. 6.2) uses a larger value of τ_A , 60 s for the SCP field program.

The FLOSSII and BPP measurements include larger stratification compared to the SCP measurements corresponding to a shift of the cospectra to even shorter time scales. Based on composited cospectra for the heat flux for the most stable conditions, we choose a 6-s averaging window (τ_A) to estimate τ . This choice omits about 10 % of the heat flux for

the most stable conditions, with the omission increasing with decreasing stability. However, the goal here is to isolate the turbulent heat flux and not to include the total flux. A larger value of $\tau_A = 36$ s will be used for examination of vertical structure across the tower layer. Therefore, the selected averaging time depends on site and on height, as determined from typical cospectral distribution of the fluxes. In general, the qualitative conclusions are not sensitive to the choice of averaging time. Exceptions are noted.

We assume that we have chosen τ_A to be close to τ , the time scale of the largest turbulent eddies, and for simplicity use only the symbol τ hereafter. Given the above choices of the averaging windows, the flow is then partitioned as

$$\phi \equiv \phi' + \bar{\phi}, \quad (1)$$

where ϕ is one of the velocity components, $\bar{\phi}$ is the average over the averaging time τ and ϕ' is the deviation from such an average. The vertical flux of ϕ for a given averaging window is then computed as $\overline{w'\phi'}$.

The mean flow corresponding to averages over τ can be further partitioned into larger scale motions, $\langle \phi \rangle$, and submeso deviations from this larger scale average, $\hat{\phi}$, such that

$$\bar{\phi} \equiv \langle \phi \rangle + \hat{\phi}. \quad (2)$$

Then the wind speed based on window-averaged components becomes

$$V \equiv (\bar{u}^2 + \bar{v}^2)^{0.5} = (\langle u \rangle^2 + 2\langle u \rangle \hat{u} + \hat{u}^2 + \langle v \rangle^2 + 2\langle v \rangle \hat{v} + \hat{v}^2)^{0.5}. \quad (3)$$

The cross-product terms on the right-hand side of Eq. 3 have no sign preference and the expected value (averaged over many windows) is zero. The quadratic terms \hat{u}^2 and \hat{v}^2 act to increase V beyond the value based on only the larger-scale averaged components ($\langle u \rangle^2$, $\langle v \rangle^2$). Even though the expected value of \hat{u} and \hat{v} averaged over many windows is zero, this submeso component enhances the wind speed because the quadratic terms do not average to zero.

3.2 Bin Averaging and Statistical Uncertainty

With weak winds, the flow is typically large non-stationary and the scatter in the relationship between the turbulence and mean flow is often large. Attempting to reduce the scatter by increasing the averaging time inadvertently captures some of the non-turbulent flow as part of the computed turbulent flow. Part of our analysis is based on averaging turbulence quantities for different intervals or bins of a mean variable such as wind speed, stratification, or velocity time changes (Sect. 3.3). This compositing is referred to as bin averaging and is symbolized with square brackets $[\phi]$. Ratios are computed from bin-averaged quantities rather than averaging the ratios directly. Bins with less than 20 samples are discarded although most bins include a large number of samples, often more than 10,000 samples. The wind and stress vectors are vector-averaged over each window of width τ and then the magnitudes of the wind speed and friction velocity for each window are computed from these averaged components. Subsequently, all of the window values are averaged separately for each bin.

For some of the SCP analysis, calculations are made separately for subdomains corresponding to the upland stations, up-valley gully stations, the side-slope stations and the valley stations. These sub-domains are chosen following Mahrt et al. (2015). The quantities based on the bin averages for each station are then averaged over the stations for each sub-region to form *sub-region averages*. Spatial averaging is not applied to the BPP network because averages over heterogeneous surfaces are difficult to interpret.

Analysis of weak-wind conditions includes significant non-stationarity and intermittency of the turbulence. As a result, existing tools for assessing the statistical significance lose

meaning, so we proceed with the understanding that uncertainty is unavoidable in the analysis of non-stationary flow.

The computed standard errors for bin averaging are generally extremely small compared to the variation between bins because of the large number of samples within each bin. The large sample size results from the small averaging width applied to several months of data. However, the uncertainty in the bin averages might be significantly underestimated by the standard error because of the dependence between samples (Leith 1973). Many of the samples for a given bin arise from adjacent windows. Lack of independence among samples is an intrinsic feature of non-stationary flows. We have computed a modified standard error based on an adjusted sample size that is reduced by the factor $(1 - \rho)/(1 + \rho)$, where ρ is the lagged correlation of the predicted variable for a separation of one window (Wilks 2006). As a numerical example for u_* computed for different bins of V , this “effective sample reduction” increases the standard error by typically 50 % for the smallest wind speeds and increases the standard error by a factor of 2–3 for the largest wind speeds. However, the adjusted standard error still remains generally small. Here, ρ was computed for the time series that falls within a given bin of V and computation of ρ for a heavily segmented time series complicates interpretation of the adjusted standard error. Furthermore, application of the adjusted sample size assumes a certain degree of statistical stationarity of the submeso motions where their local statistical characteristics do not change appreciably between different parts of the time series. This assumption of stationarity of the submeso motions is difficult to confirm.

The interpretation of the standard error is further obscured by the failure of the measurements within a given bin to approximate an ensemble average. For example, the turbulence samples within a given wind-speed bin also depend on the stratification and the non-stationarity of the flow. The environmental mean flow cannot be described by a single variable and the samples do not derive from a definable population.

Our analyses include bivariate bin averaging (Williams et al. 2013), where u_* is jointly distributed within specified intervals of two variables instead of just V . While this approach provides more insight into the behaviour of u_* sampling issues are more significant. We require only 20 samples per joint interval. Standard errors for the bivariate analyses can be as large as 10–20 % of the mean value, even without any adjustments of the standard error for dependence between samples. Consequently, the bivariate bin-averaging diagrams will be considered only as qualitative information.

3.3 Velocity Differences

The usual way to quantify the non-stationarity of the flow is to compute some measure of variability within a record of fixed length, which is large compared to τ , such as 1 h used in Liang et al. (2014) and references therein. Such methods are normally influenced by a wide range of non-turbulent motions on all time scales smaller than the record length.

Here, we relate u_* to short-term time changes in V associated with local acceleration and deceleration. Speed changes are computed centered about the i th window of the turbulence calculation, such that

$$\delta_t V(i) \equiv \overline{V(i+k)} - \overline{V(i-k)} \quad (4)$$

where $\overline{V(i+k)}$ is the average of the wind speed over the k th window after the central window (position i , Fig. 2) where u_* is computed. $\overline{V(i-k)}$ is the average over the k th window before the central window at position i . If the window averages can be assigned to points at the centre of the window, then $\delta_t V(i)$ is effectively computed over a time interval of $2k\tau$, corresponding to a time rate of change of $\delta_t V(i)/(2k\tau)$. Thus, k is a separation parameter. $\delta_t V(i)$ can be

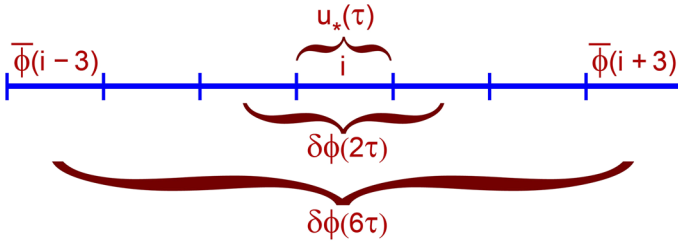


Fig. 2 Depiction of the calculation of the time difference from time series for $k = 3$ (separation of 6τ) and $k = 1$ (separation of 2τ) using centered differencing about a central window i where u_* is evaluated. ϕ represents wind speed or one of the velocity components

thought of as the differences on the time scale $2k\tau$ where motions on time scales $< \tau$ have been removed by the window averaging. Alternatively, we could examine the second-order structure function based on $\delta_t V$ that more strongly weights outlier events.

A choice of $k = 1$ could result in a form of artificial correlation between the computed turbulence and the computed non-stationary mean flow where the same structure in the time series contributes to both $\delta_t V$ and the perturbations on time scales smaller than τ . This analysis problem arises in all studies of geophysical turbulence where the variables are decomposed using a specified basis set or unweighted averaging over windows of fixed width. However, this problem is probably more significant in the weak-wind stably-stratified boundary layer where separation of the turbulent and non-turbulent motions is less clear.

We chose $k = 3$ for the separation parameter (Fig. 2), where the choice of $k > 1$ reduces the artificial correlation problem. Choice of k that is on the order of 10 or more would emphasize non-turbulent motions on time scales much larger than the largest turbulent time scales. The smaller choice of k assesses the importance of variability on those scales just larger than the turbulent scales. Non-turbulent motions on these time scales, when important, eliminate the spectral gap and change the character of the turbulence (Vercauteren and Klein 2015). The relationship between the turbulence and $\delta_t V$ for the current datasets weakens slowly with increasing k . Because the turbulence statistically increases with both flow acceleration and flow deceleration, we do not retain the sign of $\delta_t V$, unless otherwise noted.

Individual values of $\delta_t V(i)$ have little meaning because a single estimate of the local time change is not a reliable indicator of the general non-stationarity of the environment. It is only a single sample within the local flow. However, the probability of a large value of time change is greater when it is embedded within a more non-stationary environment. Therefore, we collect samples of u_* for different bins of the absolute value of $\delta_t V$ and then perform bin averaging to obtain $[u_*]$, where the square brackets refer to such bin averaging.

4 Dependence on Wind Speed and Stratification

We now briefly examine the statistical relationship between $[u_*]$ and $[V]$, written as $[u_*]([V])$. The $[u_*]$ values are always the direct bin average of the u_* magnitudes unless otherwise stated. The default width of the averaging window is 6 s for the FLOSSII and BPP measurements and 10 s for the SCP measurements. For the SCP field program, the difference between $[u_*]([V])$ for the upland stations and the valley stations is small (compare black and red lines in Fig. 3). In fact, the variation of $[u_*]([V])$ across the entire SCP domain is small, indicating that the gentle topography has little influence on this particular relationship.

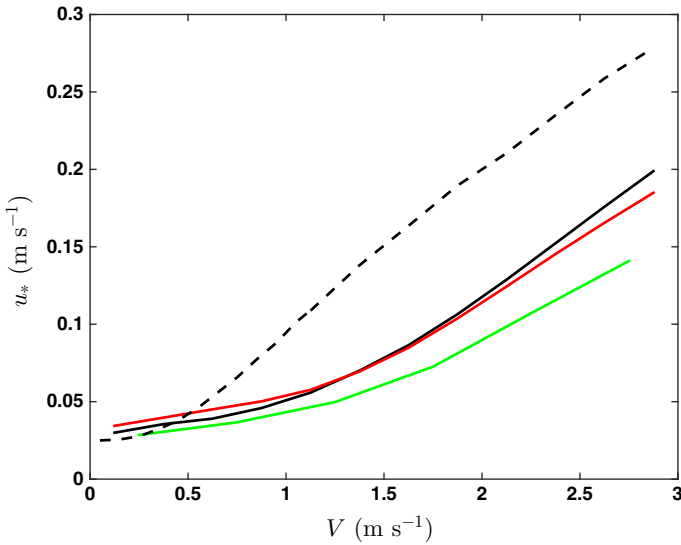


Fig. 3 Dependence of the within-bin composite of u_* on V for the SCP upland stations (*black*) and SCP valley stations (*red*), the FLOSSII tower (*green*) and BPP station C4 (*black dashed*). All observations are at 1-m height and use the short averaging window of 10 s (6 s). See Sect. 3.2 for a discussion of standard errors

For a given wind speed, u_* is smaller at the FLOSSII site compared to the SCP and BPP sites. Smaller values of u_*/V at the FLOSSII site during periods of snow cover or partial snow cover decrease the averaged values. The BPP site is characterized by values of $[u_*]/[V]$ similar to the other two field programs for the smallest wind speeds (black dashed, Fig. 3) but significantly larger $[u_*]/[V]$ than for the other field programs for larger wind speeds, perhaps reflecting the greater surface roughness upwind at the BPP site.

We now subjectively evaluate the transition wind speed V_t that roughly marks the transition between the small wind speeds, where the slope of $[u_*]/[V]$ is quite small, and the more significant wind speeds where the slope of $[u_*]/[V]$ is large. V_t occurs at about 0.3 m s^{-1} for the rougher BPP site and 0.75 m s^{-1} for the FLOSSII site and the SCP station A1 (Fig. 3).

We separately examine the relationships of u_* with V and the stratification without committing to specific dependencies, such as the dependencies in the Richardson number. For the smallest wind speeds, the impact of stratification becomes small (Fig. 4). This unexpected behaviour is discussed below. The transition wind speed for the FLOSSII site appears to increase with increasing stratification (Fig. 4) as also found at the other two sites (not shown). We have not formulated a stratification-dependent transition value because of the uncertainty in such a relationship. The reduction of u_* remains significant, on average, for $[V]$ up to 5.5 m s^{-1} (Fig. 4), which is the largest value of V with an adequate sample size for the class of largest stratification.

5 Small Wind Speeds

We now examine the dependence of the turbulence on $\delta\theta$, V and local time changes in the speed, $\delta_t V$, for small wind speeds, defined as $V < V_t$. Care must be taken when quantitatively comparing the three sites because estimation of V_t for each site is subjective. The correlations

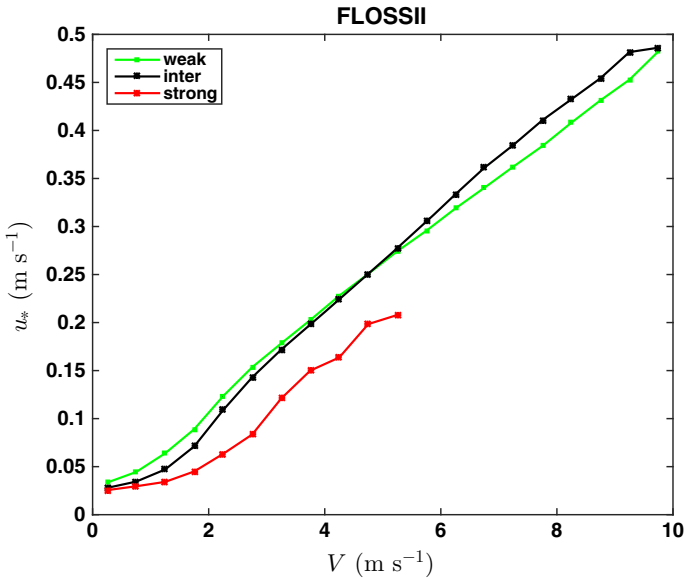


Fig. 4 Dependence of u_* on V at 1 m at the FLOSSII site for near-neutral ($\delta\theta < 0.5$ K, *green*), intermediate (0.5 K $< \delta\theta < 2$ K, *black*) and large stratification ($\delta\theta > 2$ K, *red*)

between V , $\delta\theta$, and $\delta_t V$ at a given site are small (< 0.10) so that these three characteristics of the non-turbulent flow can be considered as quasi-independent information for small wind speeds.

The variance of u_* explained by V , $\delta\theta$, and $\delta_t V$ is computed for small wind speeds as an indicator of the strength of the relationship between the turbulence and the non-turbulent flow. We use this information only qualitatively and an actual regression model is not sought. In terms of the variance of u_* explained, $\delta\theta$ is the most important variable for the SCP station A1 followed by $\delta_t V$ and then V . For the FLOSSII site, $\delta_t V$ is the most important variable followed by V and $\delta\theta$. For the BPP site, V is most important followed by $\delta_t V$ and then $\delta\theta$. The values of the variance-explained are generally statistically significant for the two most important variables, but the meaning of such statistical tests is limited for reasons discussed in Sect. 3.2. Of importance is that values of $\delta_t V$ seem essential for predicting u_* for all three sites, but that the relationship between the turbulence and the non-turbulent flow varies substantially between the three sites, as is now explored in more detail.

5.1 Joint Dependence on $\delta\theta$ and $\delta_t V$

The above tendencies for small-wind speeds are revealed in terms of the joint bivariate dependence of u_* on $\delta\theta$ and $\delta_t V$ (Figs. 5, 6, 7). Although the bias of bin averaging based on a single predictor is avoided (Williams et al. 2013), the bins for $\delta\theta$ and $\delta_t V$ must be relatively large because of sampling requirements (Sect. 3.2). The SCP field program contains a smaller number of data points for small wind speeds compared to the other two datasets.

The quantity $[u_*]$ is significantly related to $[\delta_t V]$ at all three sites and most related to $[\delta\theta]$ for station A1 at the SCP site (Fig. 5) where the square brackets now indicate bivariate bin averaging. For the FLOSSII site (Fig. 6) and the BPP site (Fig. 7), $[u_*]$ reaches a minimum value for intermediate values of $[\delta\theta]$. The greater $[u_*]$ for large $[\delta\theta]$ is unexpected. These cases

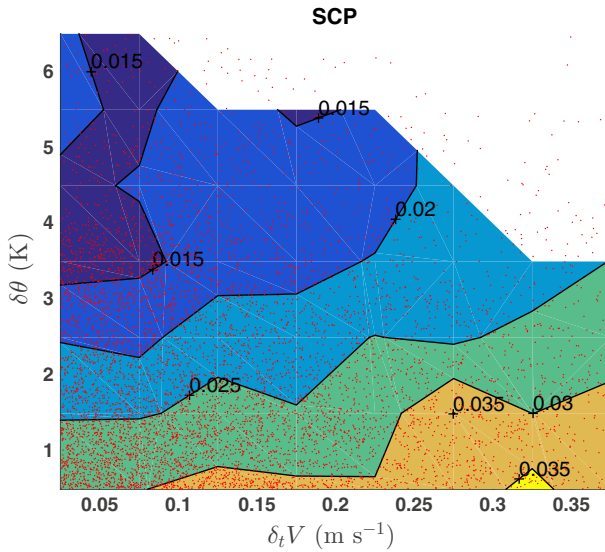


Fig. 5 Dependence of $[u_*]$ on $[\delta_t V]$ and $[\delta\theta]$ at station A1 at the SCP site for $V < V_t = 0.75 \text{ m s}^{-1}$. The interval is 0.05 m s^{-1} for $\delta_t V$ and 0.5 K for $\delta\theta$. Values are plotted at the midpoint of each box so that the point at the lower left corner of the figure corresponds to $\delta\theta$ between 0 and 0.5 K and $\delta_t V$ between 0 and 0.05 m s^{-1} . Individual window averages are shown with red dots

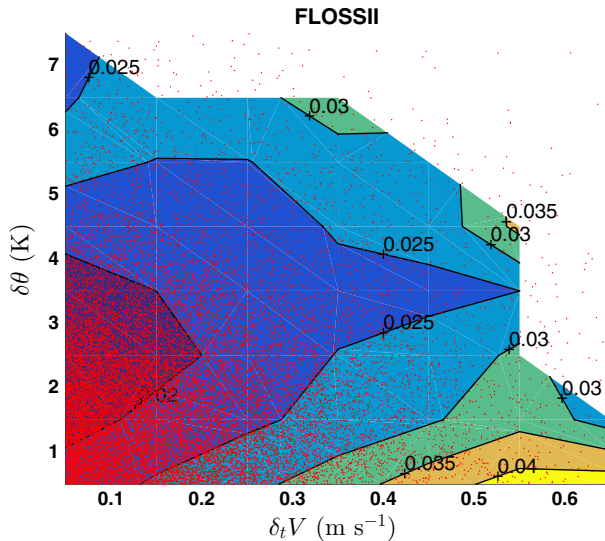


Fig. 6 Dependence of $[u_*]$ on $[\delta_t V]$ and $[\delta\theta]$ at the 1-m level at the FLOSSII site for wind speeds less than $V < V_t = 0.75 \text{ m s}^{-1}$. Axis labels refer to bin midpoints

of large $\delta\theta$ often occur with large wind-directional shear. Shallow accelerations in the lowest few metres at the BPP site are revealed by the network of sonic anemometers, continuously released fog elements and disturbances detected by the quasi-three-dimensional fine-scale temperature measurements from fibre-optic distributed temperature sensing (Zeeman et al. 2015). At station A1, u_* does not increase with large $\delta\theta$, possibly because the wind-directional

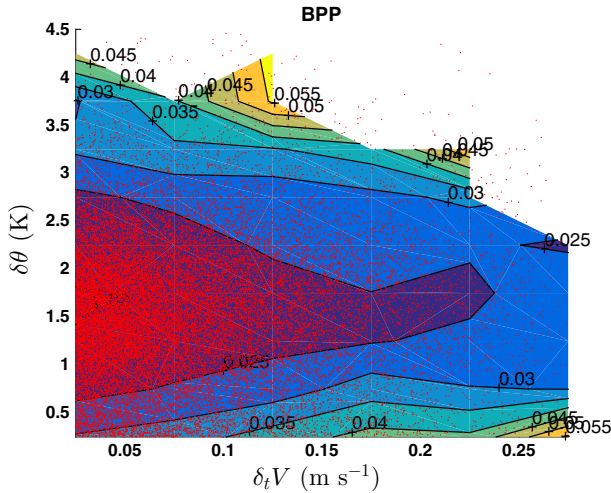


Fig. 7 Dependence of $[u_*]$ on $[\delta_t V]$ and $[\delta\theta]$ at the 1-m level at station C4 at the BPP site for $V < V_t = 0.3 \text{ m s}^{-1}$. Axis labels refer to bin midpoints. $[u_*]$ values in this diagram are smaller than at the other two sites because the transition wind speed defining the weak-wind regime is less than half of that at the other two sites

shear is small for this station, which is outside the valley and generally in the regional flow with small wind-directional shear, as is evident from the Sodar data.

These cases of largest stratification are relatively infrequent and transient because greater u_* is associated with greater mixing presumably followed by reduction of $\delta\theta$. Investigation of this speculation is complicated and probably requires a case-study approach, which is outside the scope of this study. The majority of the data points at the FLOSSII and BPP sites tend to occur with intermediate values of $\delta\theta$ where $[u_*]$ reaches a broad minimum and depends only weakly on $\delta\theta$. For this reason, the overall relationship between $[u_*]$ and $[\delta\theta]$ is relatively weak. This relatively weak relationship between $[u_*]$ and $[\delta\theta]$ for small wind speeds is also evident at the FLOSSII site, as seen on the far left side of Fig. 4.

For a fixed value of $[\delta\theta]$, $[u_*]$ increases with increasing $[\delta_t V]$ at all three sites. $\delta_t V$ is strongly skewed for the BPP and FLOSSII sites corresponding to frequent small changes in wind speed and infrequent large changes in wind speed. For the SCP site, the data points are more uniformly distributed in $\delta_t V$ - $\delta\theta$ space. The causes of these between-site differences are not understood. Thomas (2011) and Acevedo et al. (2014) found significant between-site differences in the behaviour of submeso motions, partly related to local topography and vegetation.

For wind speeds greater than the transition speed, the turbulence remains significantly correlated with $\delta_t V$, but now $\delta_t V$ is proportional to wind speed and does not contain significant independent information (not shown). The relationship between the turbulence and the stratification is more significant for wind speeds just greater than the transition value, as also observed in the CASES99 measurements (Fig. 5 of Sun et al. 2012). This maximum influence of the stratification might be related to the dependence of V_t on $\delta\theta$, not examined here.

5.2 Drainage Flow, Radiational Cooling

The SCP site differs from the FLOSSII and BPP sites in that $\delta\theta$ for $V < 0.25 \text{ m s}^{-1}$ tends to be smaller than for $0.25 \text{ m s}^{-1} < V < 1.0 \text{ m s}^{-1}$. With clear skies and weak

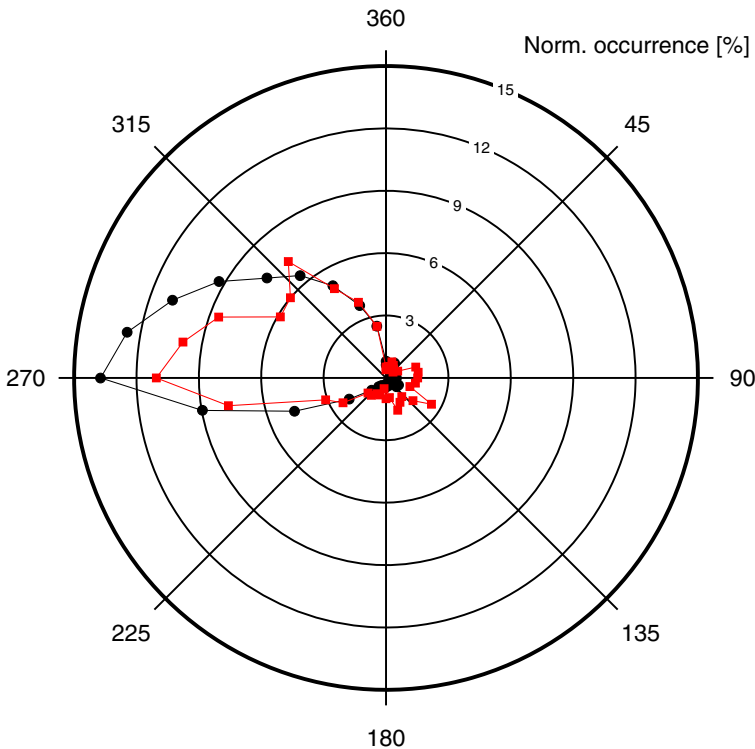


Fig. 8 The normalized occurrence of the 5-min wind direction at station A11 in the valley for $V < 1 \text{ m s}^{-1}$ for the magnitude of the surface net radiation $>50 \text{ W m}^{-2}$ (black) and for the magnitude of the surface net radiation $<30 \text{ W m}^{-2}$ (red). The number of occurrences has been normalized by the total number of samples

background flow, even weak slopes generate a drainage flow. As a result, the weakest flow at the SCP site tends to occur with cloudy conditions where a drainage flow does not develop (Mahrt et al. 2015). This tendency does not occur for the FLOSSII and BPP measurements where systematic local cold-air drainage was not evident and the very weakest flow did not tend to occur with cloudy conditions. The local slopes at the FLOSSII and BPP sites are very small and their magnitudes and directions are sensitive to the horizontal scale of assessment.

We further explore the potential influence of topography at the SCP site in terms of wind directions for 5-min averages of the 1-m wind speeds in the valley for wind speeds $<1 \text{ m s}^{-1}$. Wind directions computed over short time intervals, such as 10 s, are more erratic and are sometimes associated with short periods of nearly vanishing wind speed. With small net radiative cooling at the surface, the wind direction (Fig. 8, red) is more variable than for larger radiative cooling (black). With large radiative cooling, the wind direction is more likely to be down the valley. The differences between the two distributions are not large because of the non-stationarity of the down-valley drainage flows and because of some cases of cloudy regional flow from the west or north-west. Nonetheless, the trend shown in Fig. 8 supports the hypothesis that the decrease of stratification for the smallest wind speeds is associated with increased cloudiness (smaller radiative cooling), where drainage flow is less likely to develop.

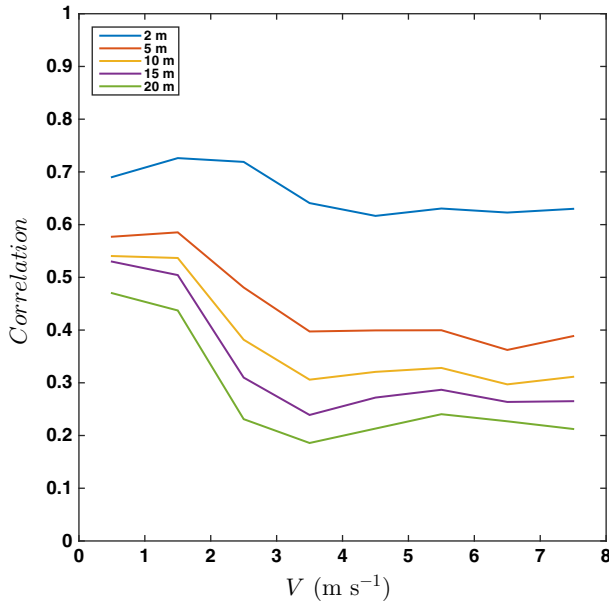


Fig. 9 Correlation of u_* at height Z (upper left legend) with the value at 1 m for 6-s averages for the FLOSSII site as a function of the 1-m wind speed

6 Vertical Structure and Accelerations

The vertical structure of the turbulence is examined with measurements from the 20-m main tower in the valley at the SCP site, the 20-m FLOSSII tower and the 12-m BPP tower.

6.1 Vertical Coherence

The vertical coherence is examined in terms of the set of correlations between the 1-m u_* values and the u_* values at each of the other levels on the tower. The vertical coherence is computed for different bins of the 1-m wind speed for the FLOSSII site. The correlation of the 1-m values of u_* , with the values of u_* at the levels above 1 m (Fig. 9), decreases with the height of the upper level, which also corresponds to increasing vertical separation distance. The vertical coherence of u_* could be due to modulation of the turbulence by submeso motions.

The vertical coherence of the turbulence unexpectedly decreases with increasing wind speed (Fig. 9). The turbulence is vertically most coherent for the smallest wind speeds, in that the correlation between u_* at the upper levels and u_* at the 1-m level is greatest. The turbulence for small wind speeds may be generated primarily by vertically coherent non-stationary submeso shear. The correlations between levels are much reduced for larger wind speeds where the impact of submeso motions is expected to be less important.

6.2 Vertical Phase

The relationship between u_* and V may be due to increased shear generation of turbulence with increased wind speed. However, the reverse process, where surface acceleration follows

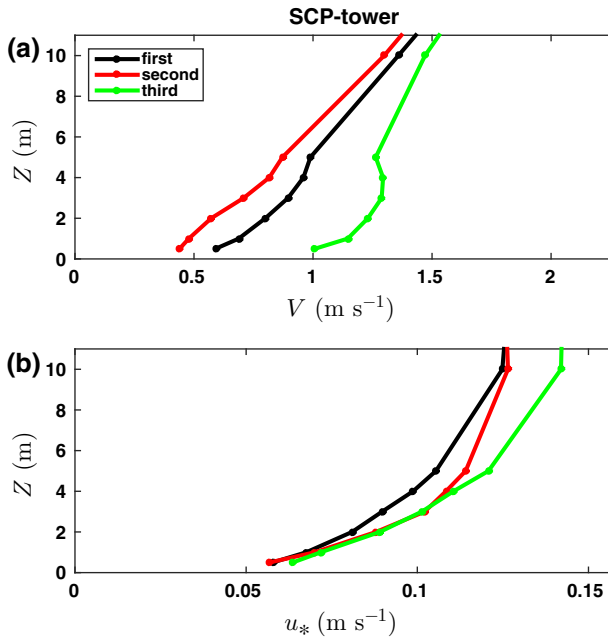


Fig. 10 **a** Composed SCP profiles of V selected from the class $V < 1.5 \text{ m s}^{-1}$ for cases where the 1-m V increased by 0.5 m s^{-1} between the second 1-min window (red) and the third 1-min window (green). Composed profiles for the first 1-min window are in black. **b** Corresponding u_*

increased downward transport of momentum, may be important near the surface, as implied in the DNS of [Shah and Bou-Zeid \(2014\)](#).

We proceed by representing the vertical structure of the time dependence in terms of three consecutive 1-min averaging windows for the SCP site and three consecutive 36-s windows for the FLOSSII and BPP sites. Numerical comparisons with fluxes at higher levels requires larger averaging windows (Sect. 3.1). Results are qualitatively similar to those based on smaller averaging windows, although the vertical coherence is smaller. Samples are selected where the 1-m wind speed increases by 0.5 m s^{-1} between the middle and last window for $V < 1.5 \text{ m s}^{-1}$ at the central window. While the results are not sensitive to the exact choice of this threshold, the intention is to capture flow in the weak-wind and transition regimes.

For the SCP site, the acceleration (compare green curve with the red curve in Fig. 10a) extends throughout the lowest 5 m and decreases at higher levels. The near-surface acceleration is preceded by a modest increase in u_* centered within the 3–10 m layer. Compare the red profile with the black profile in Fig. 10b; the enhanced downward momentum flux at the mid levels on the tower between the first and second windows apparently contributes to the subsequent flow acceleration at the lower levels between the second and third windows.

On average, surface acceleration is also preceded by increased downward momentum flux at the FLOSSII site (Fig. 11) and the BPP site (Fig. 12). The results for the BPP site are more sensitive to choice of averaging time and cut-off wind speed possibly due to the heterogeneity of the site. At the BPP site, u_* continues to increase between the second and third windows, indicating that the enhanced downward momentum flux occurs on a longer time scale compared to the other two sites. For all three sites, the depth of the event increases with increasing averaging time.

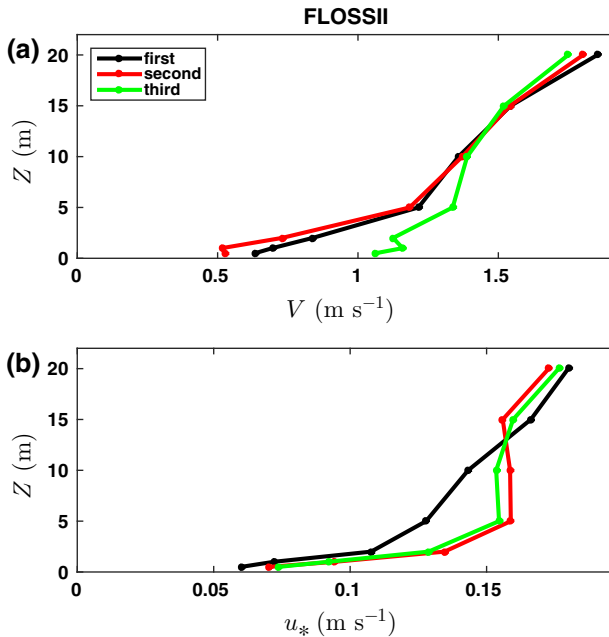


Fig. 11 **a** Composed FLOSSII profiles of V selected from the class $V < 1.5 \text{ m s}^{-1}$ for cases where the 1-m V increased by 0.5 m s^{-1} between the second 36-s window (red) and the third 36-s window (green). Composed profiles for the first 36-s window are in black. **b** Corresponding u_*

The above results provide only general tendencies. The weak-wind regime includes numerous cases where the surface u_* and V values are in-phase or where an increase in V at the surface precedes an increase in u_* . The standard error of the profiles based on conditional sampling of u_* is less than 10 % of the mean values although the standard error probably underestimates uncertainties (Sect. 3.2). In summary, for small wind speeds at all three sites, events of downward momentum flux lead to important surface flow acceleration.

Near-surface acceleration resulting from the downward transport of momentum is usually not sustainable because on longer time scales the generation of motion by the horizontal pressure gradient is generally opposed by vertical divergence of the turbulent momentum flux. Exceptions are presented in Sun et al. (2013). Indeed, as the wind speed increases to values greater than the transition value in the current datasets, the increase of u_* generally follows flow acceleration instead of preceding the flow acceleration (not shown).

7 Conclusions

Analysis of measurements from the FLOSSII, SCP and BPP field programs suggests that u_* in the weak-wind, stably-stratified, boundary layer is significantly related to small-scale submeso velocity changes ($\delta_t V$, Eq. 4). For all three sites, the turbulence for weak winds increases significantly with increasing time variability of the non-turbulent flow. Based on previous studies (see Sect. 1), the enhancement of the turbulence appears to be related to profile inflection points, non-stationary near-surface maxima of the wind speed, and wind-

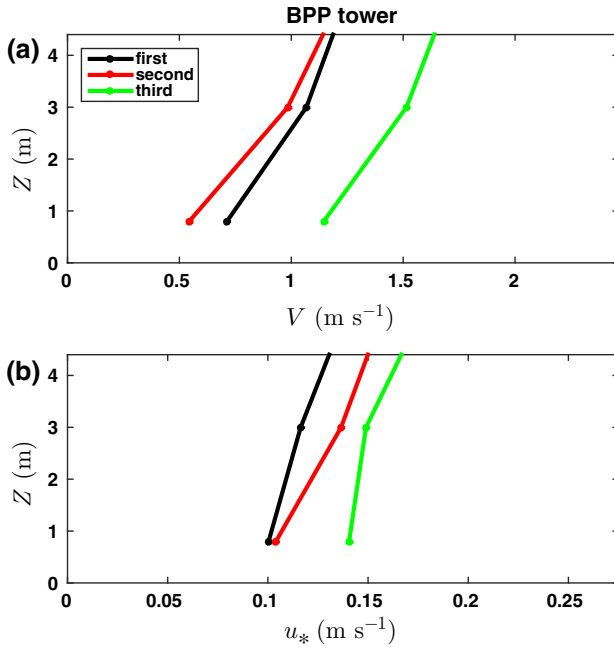


Fig. 12 a Compositing BPP profiles of V selected from the class $V < 1.5 \text{ m s}^{-1}$ for cases where the 1-m V value increased by 0.5 m s^{-1} between the second 36-s window (red) and the third 36-s window (green). Compositing profiles for the first 36-s window are in black. b Corresponding u_*

directional shear (Sect. 5.1). The friction velocity u_* , for a given wind speed, generally increases with sufficiently small stratification for all three sites.

For wind speeds smaller than the transition wind speed, an increase in the downward momentum flux often leads to surface flow acceleration while, on average, increasing wind speed does not lead to increased turbulence. In contrast, when the near-surface wind speed is larger than the transition wind speed, increased wind speed generally leads to increased u_* .

The vertical coherence of the momentum flux over the tower is largest for the weak-wind regime even though the vertical length scale of the turbulence is expected to be small. This vertical coherence is thought to result from the modulation of the turbulence by submeso motions but could also be due to bursts of downward momentum flux.

Although the above tendencies are similar at all three sites, between-site differences can be significant. The bivariate bin averaging in $\delta\theta - \delta_t V$ space indicates that the relationship between u_* and $\delta\theta$ for weak winds is complex at two of the three sites where u_* unexpectedly increases with increasing large stratification. Such an increase of u_* involves a relatively small number of data points mainly associated with large wind-directional shear for large $\delta\theta$. Consequently, the roles of the wind speed and stratification for this particular case are not adequately accommodated by a single non-dimensional combination, such as the bulk Richardson number.

The usual inverse relationship between the wind speed and stratification is observed for the FLOSSII and BPP field programs, but breaks down for very small wind speeds in the SCP domain. Extremely small wind speeds are more likely to occur with cloudy conditions and thus with smaller averaged stratification. With clear skies and surface radiational cooling,

the gentle slopes at the SCP site generate cold-air drainage and thus prevent extremely weak winds.

These results must be treated with caution because it is difficult to analyze turbulence in the non-stationary weak-wind regime (Sect. 3). In addition, the development of turbulence events is difficult to assess from fixed towers because the turbulence events may have been generated upwind where the submeso flow was different. The use of spatially dense observations, such as fibre-optic distributed temperature sensing, would improve understanding of this problem.

Acknowledgments This project received support from Grants AGS-1115011 and AGS 0955444 from the National Science Foundation. The measurements for the SCP and FLOSSII field programs were provided by the Integrated Surface Flux System of the Earth Observing Laboratory of the National Center for Atmospheric Research.

References

- Acevedo O, Costa F, Oliveira P, Puhales F, Degrazia G, Roberti D (2014) The influence of submeso processes on stable boundary layer similarity relationships. *J Atmos Sci* 71:207–225
- Anson C, Mellado J (2014) Global intermittency and collapsing turbulence in a stratified planetary boundary layer. *Boundary-Layer Meteorol* 153:89–116
- Finnigan J (1999) A note on wave-turbulence interaction and the possibility of scaling the very stable boundary layer. *Boundary-Layer Meteorol* 90:529–539
- Galperin B, Sukoriansky S, Anderson P (2007) On the critical Richardson number in stably stratified turbulence. *Atmos Sci Lett* 8:65–69
- Garratt JR (1990) The internal boundary layer—a review. *Boundary-Layer Meteorol* 50:171–203
- Garratt JR (1994) *The atmospheric boundary layer*. Cambridge University Press, Cambridge, UK, 316 pp
- Hicks B, Pendergrass W III, Vogel CA, Keener RN Jr, Leyton SM (2014) On the micrometeorology of the Southern Great Plains I: legacy relationships revisited. *Boundary-Layer Meteorol* 151:389–405
- Kang Y, Belušić D, Smith-Miles K (2015) Classes of structures in the stable atmospheric boundary layer. *Q J R Meteorol Soc* 141:2057–2069
- Leith C (1973) The standard error of time-averaged estimates of climatic means. *J Appl Meteorol* 12:1066–1069
- Liang J, Zhang L, Wang Y, Cao X, Zhang Q, Wang H, Zhang B (2014) Turbulence regimes and the validity of similarity theory in the stable boundary layer over complex terrain of the Loess Plateau. *J Geophys Res China*. doi:10.1002/2014JD021510
- Mahrt L (2010a) Common microfronts and other solitary events in the nocturnal boundary layer. *Q J R Meteorol Soc* 136:1712–1722
- Mahrt L (2010b) Variability and maintenance of turbulence in the very stable boundary layer. *Boundary-Layer Meteorol* 135:1–18
- Mahrt L, Thomas CK, Richardson S, Seaman N, Stauffer D, Zeeman M (2013) Non-stationary generation of weak turbulence for very stable and weak-wind conditions. *Boundary-Layer Meteorol* 177:179–199
- Mahrt L, Sun J, Oncley SP, Horst TW (2014) Transient cold air drainage down a shallow valley. *J Atmos Sci* 71:2534–2544
- Mahrt L, Sun J, Stauffer D (2015) Dependence of turbulent velocities on wind speed and stratification. *Boundary-Layer Meteorol* 155:55–71
- Shah S, Bou-Zeid E (2014) Direct numerical simulations of turbulent Ekman layers with increasing static stability: modifications to the bulk structure and second-order statistics. *J Fluid Mech* 760:494–539
- Soler M, Udina M, Ferreres E (2014) Observational and numerical simulation study of a sequence of eight atmospheric density currents in northern Spain. *Boundary-Layer Meteorol* 153:195–216
- Sorbjan Z, Grachev A (2010) An evaluation of the flux–gradient relationship in the stable boundary layer. *Boundary-Layer Meteorol* 135:385–405
- Sun J, Mahrt L, Banta RM, Pichugina YL (2012) Turbulence regimes and turbulence intermittency in the stable boundary layer during CASES-99. *J Atmos Sci* 69:338–351
- Sun J, Lenschow D, Mahrt L, Nappo C (2013) The relationships among wind, horizontal pressure gradient and turbulent momentum transport during CASES99. *J Atmos Sci* 70:3397–3414
- Sun J, Mahrt L, Nappo C, Lenschow D (2015) Wind and temperature oscillations generated by wave–turbulence interactions in the stably stratified boundary layer. *J Atmos Sci* 71:1484–1503

- Tennekes H, Lumley JL (1972) *A first course in turbulence*. The MIT Press, Cambridge, 300 pp
- Thomas C (2011) Variability of sub-canopy flow, temperature, and horizontal advection in moderately complex terrain. *Boundary-Layer Meteorol* 139:61–81
- Thomas C, Smoot AR (2013) An effective, economic, aspirated radiation shield for air temperature observations and its spatial gradients. *J Atmos Ocean Technol* 30:526–537
- Thomas C, Kennedy A, Selker J, Moretti A, Schroth M, Smoot A, Tufillaro N (2012) High-resolution fibre-optic temperature sensing: a new tool to study the two-dimensional structure of atmospheric surface-layer flow. *Boundary-Layer Meteorol* 142:177–192
- Thomas C, Martin JG, Law BE, Davis K (2013) Toward biologically meaningful net carbon exchange estimates for tall, dense canopies: multi-level eddy covariance observations and canopy coupling regimes in a mature douglas-fir forest in oregon. *Agric For Meteorol* 173:14–27
- van Hooijdonk I, Donda J, Clercx H, Bosveld F, van de Wiel B (2015) Shear capacity as prognostic for nocturnal boundary layer regimes. *J Atmos Sci* 72:1518–1532
- Vercauteren N, Klein R (2015) A clustering method to characterize intermittent bursts of turbulence and submeso motions interaction in the stable boundary layer. *J Atmos Sci* 72:1504–1517
- Wilks DS (2006) *Statistical methods in the atmospheric sciences*. Academic Press, New York, 627 pp
- Williams A, Chambers S, Griffiths S (2013) Bulk mixing and decoupling of the stable nocturnal boundary layer characterized using a ubiquitous natural tracer. *Boundary-Layer Meteorol* 149:381–402
- Zeeman MJ, Selker JS, Thomas C (2015) Near-surface motion in the nocturnal, stable boundary layer observed with fibre-optic distributed temperature sensing. *Boundary-Layer Meteorol* 154:189–205